Acta Materialia 105 (2016) 338–346

Contents lists available at ScienceDirect

Acta Materialia

journal homepage: www.elsevier.com/locate/actamat

Full length article

Time-resolved synchrotron tomographic quantification of deformation during indentation of an equiaxed semi-solid granular alloy

B. Cai [a, b], P.D. Lee [a, b, *], S. Karagadde [a, c], T.J. Marrow [d], T. Connolley [e]

[a] School of Materials, University of Manchester, Manchester, M13 9PL, UK
[b] Research Complex at Harwell, Rutherford Appleton Laboratory, Harwell, OX11 0FA, Oxfordshire, UK
[c] Department of Mechanical Engineering, Indian Institute of Technology Bombay, Mumbai, 400076, India
[d] Department of Materials, University of Oxford, Oxford, OX1 3PH, UK
[e] Diamond Light Source Ltd., Harwell Science and Innovation Campus, OX11 0DE, Didcot, UK

ARTICLE INFO

Article history:
Received 23 October 2015
Accepted 15 November 2015
Available online 9 January 2016

Keywords:
Granular materials
Semi-solid
Indentation
X-ray tomography
Digital volume correlation

ABSTRACT

Indentation is a well-established technique for measuring mechanical properties, such as hardness and creep, in solid materials at a continuum level. In this study, we performed indentation of a semi-solid granular alloy with an equiaxed dendritic microstructure. The resulting microstructural effects were quantified using a novel thermo-mechanical setup combined with 4D (three spatial dimensions plus time) synchrotron tomography and digital volume correlation. The experiments not only revealed the multitude of deformation mechanisms occurring at a microstructural level, (e.g. dilatancy, liquid flow, macrosegregation, shrinkage voids, and intra-granular deformation), but also allowed quantification of the evolution of the strain fields within the material. The resulting methodology is a powerful tool for assessing the evolution of localized deformation and hence material properties.

1. Introduction

Indentation is one of the standards for probing local plastic deformation and characterizing the hardness and other material properties of solid samples [1–6]. Indentation has also been employed to investigate high temperature properties such as creep [7–9] and to obtain the deformation response of granular ensembles [10,11]. Granular media (e.g. sands, magma, sugar) consist of solid grains and pores filled with gas or liquid [12]. The behaviour of a granular material under indentation by a rigid body is of vital importance to a wide range of applications, including soil-machine interaction [13], the deformation of volcanic edifices by viscous magma [14], and semi-solid metal fabrication [15,16].

The deformation zone generated by indentation is determined mostly from the final-deformation state, providing minimal information on the dynamic evolution. This dynamic process includes two important aspects: (1) the microstructural changes induced by localized deformation and (2) the distribution and evolution of the strain fields as deformation proceeds. A considerable challenge is presented when attempting to map the complicated time-dependent evolution of microstructures, material flow and stress/strain fields induced by the indenting rigid body due to sample opacity. Particle tracking methods based on optical images (which is inherently a 2D process) [17–19], confocal microscopy [11] and magnetic resonance techniques [12] have been developed to partially overcome these challenges; as such, they can provide near-surface material flow gradients and/or strain evolution but are limited in their ability to determine the dynamics on a microstructural level. Recently, the ability to resolve microstructures in optically-opaque materials combining X-ray tomography and digital volume correlation (DVC) to quantify displacement field has been shown to be a useful approach to investigate sub-indentation deformation processes [4,20], although time-dependent information (e.g. velocity field) has not yet been obtained.

The rheological behaviour of semi-solid alloys has attracted significant attention recently (e.g. Refs. [21–28]). The complex interactions of solid–solid and solid–liquid phases have displayed not only characteristic granular behaviour [21,23,28,29] but also intra-granular deformation [21,25,30]. Dilatancy, an inherent

* Corresponding author. School of Materials, University of Manchester, Manchester, M13 9PL, UK.
E-mail address: peter.lee@manchester.ac.uk (P.D. Lee).

http://dx.doi.org/10.1016/j.actamat.2015.11.028

deformation response of granular materials, has been shown to occur in semi-solid alloys [21,26]. Meanwhile, strain localization during semi-solid deformation has also been observed in some recently studies using uniaxial compression [21] and a direct shear cell [31]. However, the relationship between localized deformation and dilatancy has not been directly quantified. Indentation loading is known to generate a highly localized deformation zone in the vicinity of the indenter [1,4,32]. Hence indentation may be an ideal approach to reveal the correlation between dilatancy and inhomogeneous deformation as long as we can quantitatively assess both simultaneously. In addition, indent loading is of practical relevance for advanced casting techniques, because mechanical forces are both imposed on the surface and also penetrate deep into the components [15,16]. Discrete finite element models [33] and discrete element models [22] are currently being developed to address micro mechanic of semi-solids, which crucially requires well-designed experiments with both microstructure responses and strain evolution for their validation.

Here we report the combined use of high speed synchrotron X-ray tomography, digital volume correlation (DVC), and a bespoke *in situ* indentation rig with a resistance furnace to resolve the formation of deformation zones during indentation loading in 4D, offering a new perspective for micro mechanical tests of granular materials. Secondly, by indenting a semi-solid equiaxed dendritic Al–Cu alloy with a solid fraction of 72%, this study demonstrates that dilatancy is a direct response of localized deformation, leading in turn to liquid migration, solute-segregation and solidification porosity. This study demonstrates the advantage of combining multiple complementary techniques to gain new insights into the mechanics of deforming semi-solid granular materials.

2. Materials and methods

A cylindrical sample (3 mm diameter and 3 mm height) of Al-15wt.%Cu was placed inside a boron nitride holder with inner diameter of 3 mm and wall thickness of 1 mm. A bespoke thermo-mechanical rig ("P2R") was used together with a split open resistance furnace (Fig. 1) [21,34]. The indenter was a 30° flat-tipped (~250 μm diameter) cone made of alumina.

The experiments were performed at Diamond Light Source beamline I12 [35] with 53 keV monochromatic X-ray beam and coupled to a Vision Research Miro 310M camera via an imaging chain. The pixel size was 4 μm. The sample was heated to 560 ± 2 °C and held for 10 min, creating a semi-solid sample with a solid volume fraction (f_s) of 72%. The deformation was then started at a speed of 5 μm/s. High speed tomographic scans were taken in intervals of 9 s, acquiring one 3D dataset with 900 projections in 9 s over a sweep of 180°. Nine datasets were recorded in total, during which the indenter travelled a distance of 720 μm. Another single dataset was acquired at the end of the deformation process, after a total penetration of 1500 μm. Then the sample was cooled with the furnace turned off. A final dataset was recorded when the sample reached room temperature.

3D reconstructions were performed using the *Savu* system [36,37]. A 3D median filter followed by a non-local diffusion filter, using Avizo 8 (FEI VSG, France), was used to reduce noise. The liquid and pore phases were segmented from the solid using the Otsu threshold method [38]. The thickness of the liquid channels was measured using BoneJ [39]. The movement of individual grains (rotation angle and translation magnitude) at a representative vertical plane was determined via an image registration scheme (Avizo 8, FEI VSG, France). Due to the complexity of the dendritic structure and limited image contrast, automatic isolation of the individual dendrites could not be completed. Instead, a careful manual separation using visual observations was performed. A

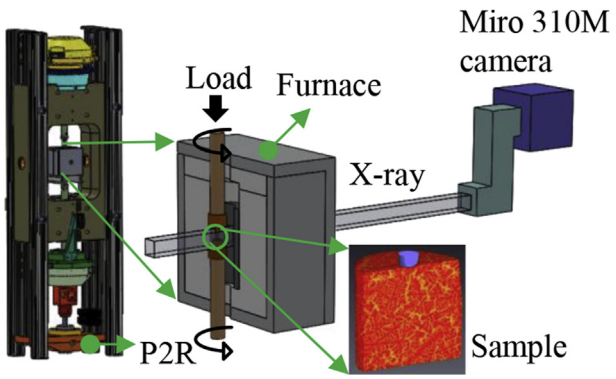

Fig. 1. Schematic of the experimental apparatus.

registration algorithm with affine transformation and an iterative optimization (Avizo 8, FEI VSG, France) was then applied to track the movement (translation and rotation) of the same dendrite from an indentation depth of $I = 0$–720 μm at the representative vertical plane.

DaVis Strain Master Version 8.1 was used to measure the 3D displacement fields. The DVC procedure is described in Ref. [21]. Here, a subset of 64 × 64 × 64 pixels with 50% overlap was used. The resulting spatial resolution of the displacement field is 32 pixels, corresponding to 128 μm. The displacement fields between successive tomographic datasets were integrated through the data series to calculate the accumulated displacement fields ($\mathbf{u}_i, i = x, y, z$). The velocity was obtained using $\mathbf{V}_i = \frac{\mathbf{u}_i}{\Delta t}$, where u_x, u_y, u_z denote the displacement field at x, y, z direction, respectively, and V_x, V_y, V_z represent the velocity component at x, y, z direction.

The accumulated displacement fields were also used to calculate the strain tensor ($\boldsymbol{\varepsilon}_{\mathbf{ij}}$, $i, j = x, y, z$) by a finite difference method. The strain tensor was further decomposed to octahedral normal strain (ε_n) and shear strain (ε_s), respectively.

3. Results and discussion

The influence of deformation zone formation on the microstructure is presented both qualitatively and quantitatively. The real-time tomographic imaging of indentation processes at high temperature and semi-solid state allowed us to quantify grain motion, the degree of dilatancy and associated liquid flow, together with strain evolution.

3.1. Grain motion

Fig. 2 shows a typical sequence of 2D, longitudinally-sectioned (y-z) tomographic slices recorded during the indentation of the semi-solid Al–Cu sample. Four different penetration depths ($I = 0$, 90, 360 and 720 μm) are shown in Fig. 2a to d, respectively. Supplementary movie S1 shows the full indentation process. The Al-rich dendrites are darker grey and the Cu-rich liquid is white, due to the difference in X-ray attenuation of the two phases (shown in reverse contrast, where lighter colour indicates denser materials). The initial equiaxed dendritic microstructure is clearly distinguishable (Fig. 2a). After 90 μm of indentation, Fig. 2b, the grains directly below the indenter were slightly displaced, causing the surrounding grains to move as well; this was buffered by the thin layers of intergranular liquid. With further deformation, the movement of grains continued (Fig. 2c and d, and more clearly shown in the Supplementary movie S1). Such movement indicates that a force chain was built up through the contact points of grains.

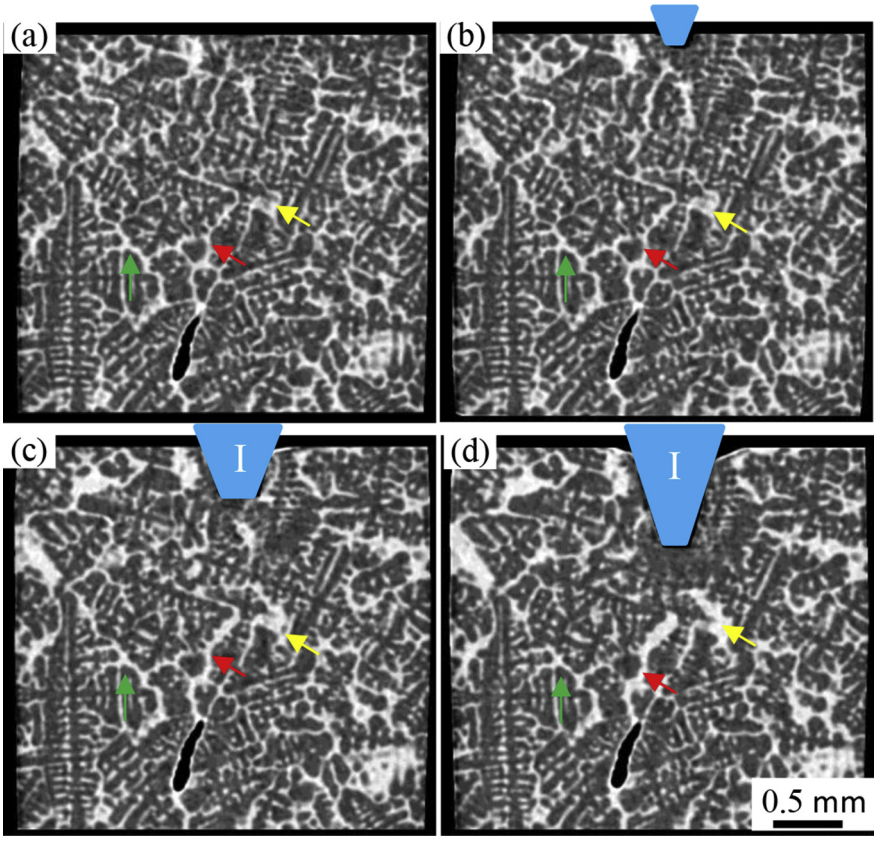

Fig. 2. Microstructural development of the semi-solid Al-15wt%Cu ($f_s = 72\%$) indented at a displacement rate of 5 μm/s at a depth of (a) $I = 0$ μm; (b) $I = 90$ μm; (c) $I = 360$ μm; and (d) $I = 720$ μm.

Supplementary videos related to this article can be found at http://dx.doi.org/10.1016/j.actamat.2015.11.028.

By tracking of the 34 dendrites in this slice (Fig. 2a) from $I = 0$–720 μm, the translation magnitudes (Fig. 3a) and rotation angles (Fig. 3b) were measured. Although the system is three-dimensional, this measurement in two dimensions can still provide a reasonable approximation to clarify how grains arrange themselves as a result of imposed deformation. As shown in Figs. 3a and b, the indentation triggered both translation and rotation of individual grains. Each grain moved differently, which is primarily due to inhomogeneous deformation imposed by the indentation loading. Interestingly, these equiaxed grains with complex morphologies only rotate by a few degrees, showing how important morphology and solid volume fraction are in granular flow. For example, although dendrite A was moved by a magnitude of ~100 μm, it only rotated about 3° anti-clockwise.

3.2. Dilatancy effects

In addition to the observation of grain movement, the channels between grains changed significantly, as shown in Fig. 2. The opening-up of liquid channels (LCs) can be directly observed in Fig. 2 in 2D, but is further validated in Fig. 4. Specifically, Fig. 4a to d shows the complementary transverse cross-sectional (x-z) slices at different indentation depths ($I = 0$, 90, 360 and 720 μm). Although the LCs between the second dendrite arms appeared to remain unchanged, the interdendritic space enlarged with increasing indentation depth.

To quantify dilatancy, a medial axis method [39] was applied to the segmented liquid channels. The resulting LC thickness distributions are shown in 3D in Fig. 4e–h (supplementary movie S2). Note due to the imaging system resolution for the chosen field of view, thin liquid films less than about 3 pixels (12 μm) could not be detected. Initially, they are homogeneously distributed (Fig. 4e). With 90 μm of indentation, the thickness of the LC close to the indenter surface increased slightly. With more deformation ($I = 360$ μm), the opening of the LC became obvious and propagated deep into the sample, growing vertically downwards. When the indenter was pushed even further (720 μm, Fig. 4g), large interconnected pocket-like channels appeared (red colour in the web version).

Supplementary videos related to this article can be found at http://dx.doi.org/10.1016/j.actamat.2015.11.028.

Fig. 5 presents the cumulative distribution of liquid channel thickness. The following key inferences can be made from the measurement of channel thickness:

(i) The average thickness of LCs increased only slightly, from a width of 37–50 μm as the indenter went from 0 μm to 720 μm; this is most likely due to the LCs between second dendrite arms dominating and remaining unchanged during deformation.
(ii) The volume fraction of LCs with thicknesses greater than 60 μm increased significantly from 4.7% to 17.4%. In addition, the maximum thickness increased continuously from 111 to 180 μm. This illustrated the substantial opening of the interdendritic channels.

In summary, a considerable and highly localized increase in inter-granular spacing was observed as deformation proceeded,

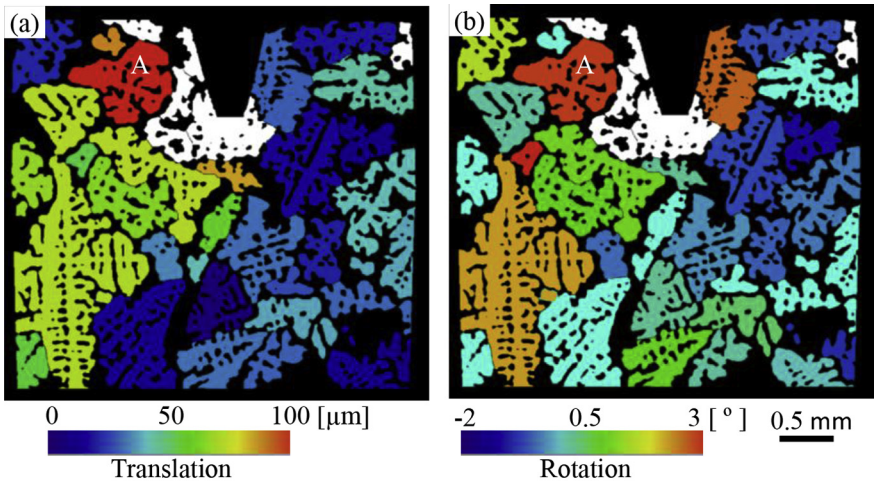

Fig. 3. (a) Translation amplitude and (b) rotation angle of individual grains at $I = 720$ μm (dendrites in white could not be measured).

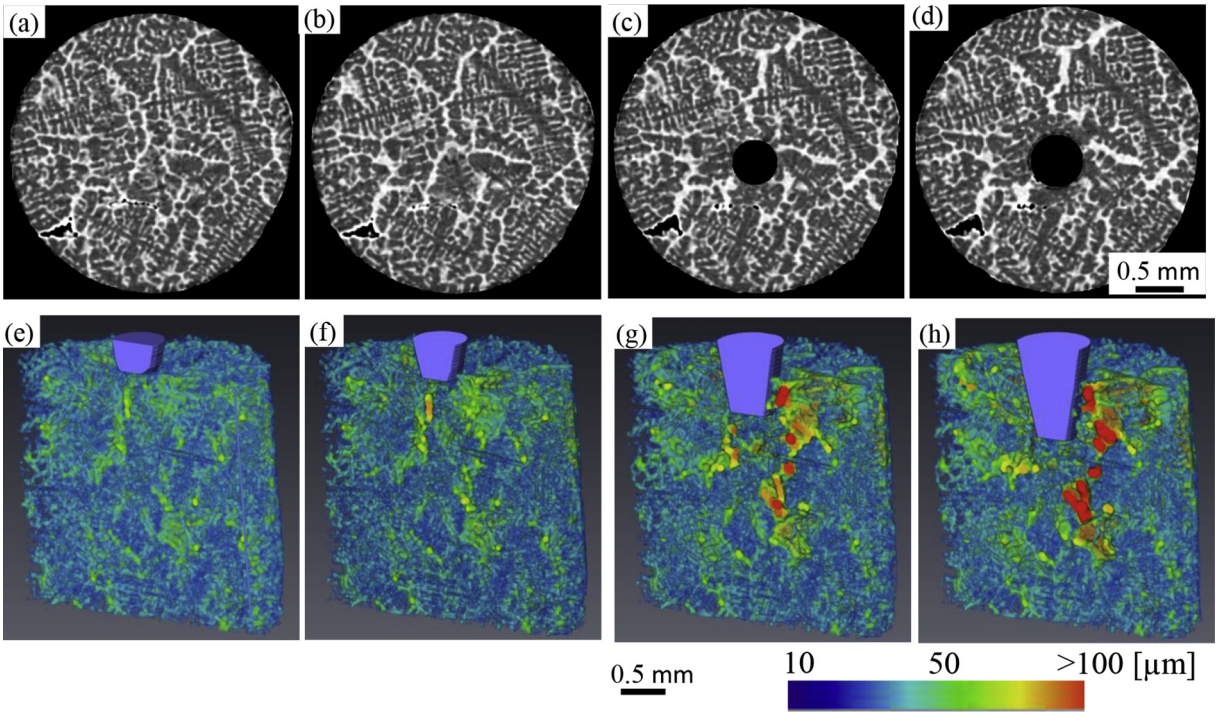

Fig. 4. (a) to (d) Transverse slices at sample height of 360 μm, (e) to (h) Section view showing the distribution of liquid channel thickness at: (a) and (e) $I = 0$ μm; (b) and (f) $I = 90$ μm; (c) and (g) $I = 360$ μm; (d) and (h) $I = 720$ μm.

attributable to dilatancy. Dilatancy is one of the fundamental microstructural responses of deforming granular materials [40,41]. In our case, the dilated LCs are directly related to the inhomogeneous deformation field. The inhomogeneous deformation induced by indenting appeared to propagate through specific paths or force chains, causing certain grains to move unevenly, increasing its channels and void spaces which also appeared to be inhomogeneous located in the vicinity of the indenter. These enlarged inter-connected channels can be regarded as percolating paths linking void spaces [42] and would be expected to change the permeability in the system [25]. It has been shown that rotation of particles plays a determining role in deciding the degree of dilatancy [43]. Tomoya et al. [43] found that the liquid-filled channels increased greatly within the shear plane although solid grains only rotated by a few degrees. This study also confirms that only a slight rotation of grains is required to induce significant dilatancy. The dilatancy in dense semi-solid alloys subjected to localized deformation is relevant and essential to our understanding of solid–granular interaction, benefiting a wide variety of industrial applications which involve surface indentation of granular materials [13]. This could also provide us with essential understanding of the nucleation mechanism for atomic-scale defects such as dislocations [11].

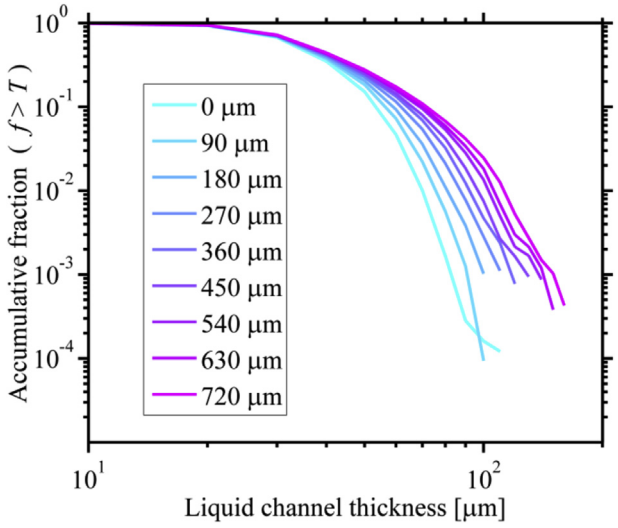

Fig. 5. Cumulative liquid channel thickness distributions at various indentation depths (T is the liquid channel thickness).

3.3. Liquid migration

Dilatant shearing of grains caused grain separation to increase, locally reducing the pressure in that liquid region, and resulting in segregation of solute enriched interdendritic liquid from other areas into the widened interdendritic spaces. Fig. 6 shows the variation in liquid fraction (averaged over 80 μm) along the deformation axis at various depths, normalized by sample height. The liquid fraction increased (i.e. accumulation of liquid) in the upper part of the sample with increasing deformation, while there was depletion of liquid in the lower region (Fig. 6). Thus, the dilatancy in the upper region draws solute enriched interdendritic liquid from the lower region, causing macrosegregation. When the solid–liquid mush is under compressive stress, the porous semi-solid mixture is compacted as the liquid is driven out. On the other hand, when the mush is sheared, the solid particles rearrange themselves (dilatancy), and draw liquid from the surrounding regions to compensate for the increased volume.

A small region (Zone D in Fig. 6a) shows an increase of liquid fraction at the beginning of deformation (from I = 0–350 μm) then a reduction. Initially when the indenter was far from Zone D, the force was transmitted to the grains in Zone D, shearing them apart. As the indenter travelled closer to this zone, more compressive deformation was imposed, thus draining the liquid out. Fig. 6b to d shows a series of sectioned 3D views of the tomographic volumes. The LC marked by the green (in the web version) arrow (in Fig. 6b to d) was initially open (Fig. 6a to b), but closed at the latter stage (from Figs. 6c and d). This shows that changes of deformation conditions can alter liquid flow tendency. Such observations are important, for instance, in understanding the responses of semi-solid alloys when the deformation conditions change [44].

3.4. Defect formation

The sample was indented to a total depth of 1500 μm, and then the furnace was allowed to cool whilst tomography was continued. Fig. 7a shows the distribution of pores at the end of deformation, but while the sample is still a semi-solid. Two types of pores were observed; irregularly-shaped ones located on the left side of the indenter in Fig. 7a and then one globular pore on the right side. The

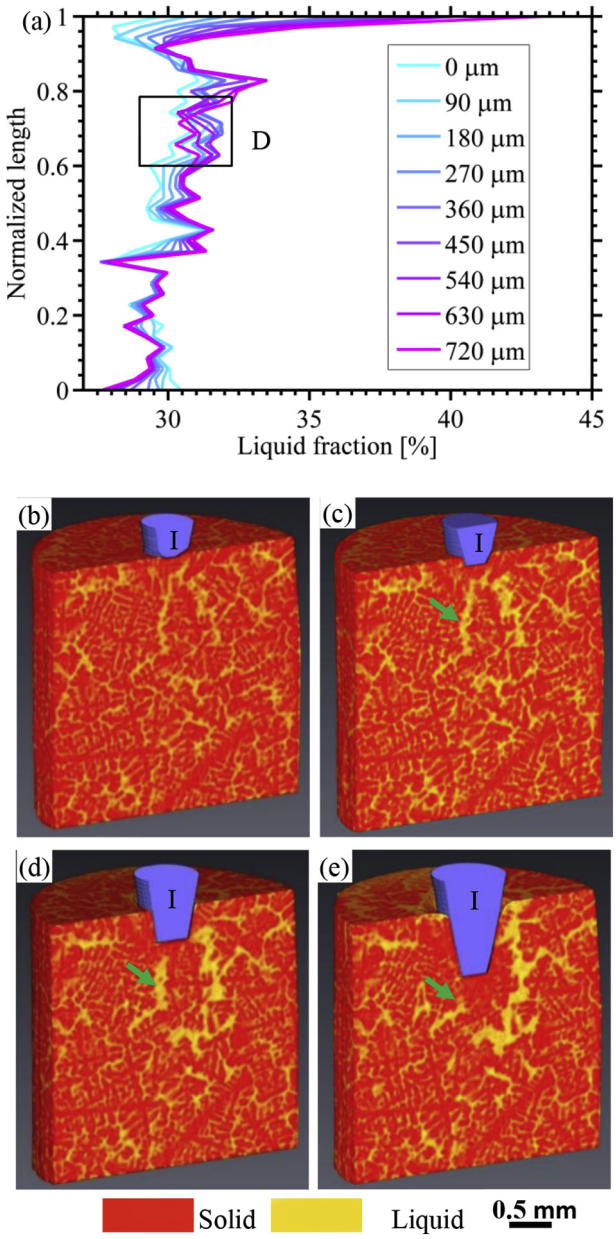

Fig. 6. (a) Variation of liquid fraction versus the sample height; (b) to (e) subsequent stages of indentation: (b) I = 0 μm; (c) I = 90 μm; (d) I = 270 μm; (e) I = 720 μm.

latter was probably a gas pore formed during the isothermal holding period. Fig. 7b shows the pores present in the solidified sample. Clearly, there are many more pores in the solidified sample than there were in the semi-solid sample. The number of pores increased from 33 to 479, while the total volume of pores increased from 0.056 to 0.106 mm^3. Although in the solidified sample, most of the pores were smaller in size, there were a few larger pores with irregular shape, due to not only the growth of the existing pores in the semi-solid sample, but also the initiation and growth of fresh pores (marked by black arrows in Fig. 7b). This increase in porosity in the solidified microstructure can be explained by inadequate liquid feeding [45] - the dilatant response of the semi-solid structure greatly increased the size of inadequately-fed liquid pockets leading to larger pores forming upon solidification. This has previously been hypothesized to be one mechanism through which pores form within the shear band of twin roll casted components

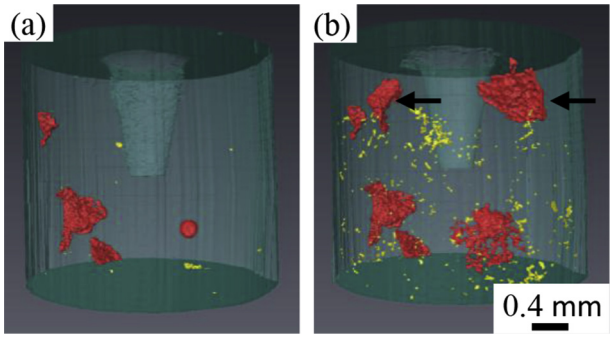

Fig. 7. Porosity (a) in the semi-solid state at an indentation depth of $I = 1500$ μm, (b) in the solidified state after complete deformation. Colours are indicative of the size of the pore (yellow for pore volume smaller than 6×10^5 μm^3, red larger than 6×10^5 μm^3). (For interpretation of the references to colour in this figure legend, the reader is referred to the web version of this article.)

[44,46] and deformed partially solidified alloys [26].

3.5. Intra-granular deformation

During the indention, we observed grain movement as well as plastically deforming grains directly below the flat tip of the indenter (Fig. 8a–e). A dendrite tip (A) just underneath the indenter's flat surface was compacted locally increasing the solid fraction. Another dendrite tip (B) showed similar behaviour although this happened later. As shown in Fig. 8e, it appears that A and B were compressed together. A dead-metal zone directly below the indenter has been observed when indenting solid samples [47] or hard particles [10,48] using a flat punch indenter. This is due to the no-slip condition present on the indenter's flat tip, which keeps the material below the indenter's flat surface locked, i.e. the materials move at the same speed as the indenter [47,48]. Here, although the dendrites were also locked, the coefficient of friction between the indenter and the semi-solid is unknown and the liquid fraction may act like a lubricant, so the "no slip" condition may not strictly apply. Additionally, the dendrites are more easily deformed, becoming compressed like a sponge and driving out the interdendritic liquid.

Local plastic deformation of grains can also be observed. For example in Fig. 8f–j, the primary dendrite trunk is bent significantly. The force was transmitted to this dendrite from the indenter, not only driving the dendrite to downward, but also bending it mechanically, potentially generating variations in its crystallographic orientation. The bending happened during the later stages of indentation when the dendrites became more entangled and flow more difficult. Although the bending of dendrites in the mushy zone has been experimentally observed in several systems [21,49,50], current models of semi-solid deformation during solidification has not simulated this phenomena [24,51]. The models developed by Yamaguchi and Beckermann [24,52] simulated the change of crystallographic orientation of a solidifying dendrite due to deformation; hence their model may be able to provide a way of numerically simulating the dendrite bending phenomena. Here we have shown that in addition to the dilatancy induced by grain motion, strains can also be accommodated by intragranular deformation.

3.6. Velocity and strain field

The strain localization, quantified by Digital Volume Correlation, is shown in Fig. 9. Fig. 9a–d shows the progression of the velocity field as a series of quiver plots from the start of indentation to a depth of 720 μm (Supplementary movie S3). The grains moved away from the indenter radially, with those close to the indenter moving faster than those further away. The localized velocity at the beginning of indentation deformation is highest, decreasing as force chains are formed and the strain is spread over a larger area.

Supplementary video related to this article can be found at http://dx.doi.org/10.1016/j.actamat.2015.11.028.

Positive values of normal strain (ε_n, Fig. 9) represent dilation (volume expansion) of the sample, while negative values indicate shrinkage. Initially ($I = 90$ μm), a large region of dilation with less than 2% of positive normal strain formed under the indenter (Fig. 9a). Away from the indenter, negative ε_n was prevalent, indicating the compression of the solid skeleton. At 180 μm of

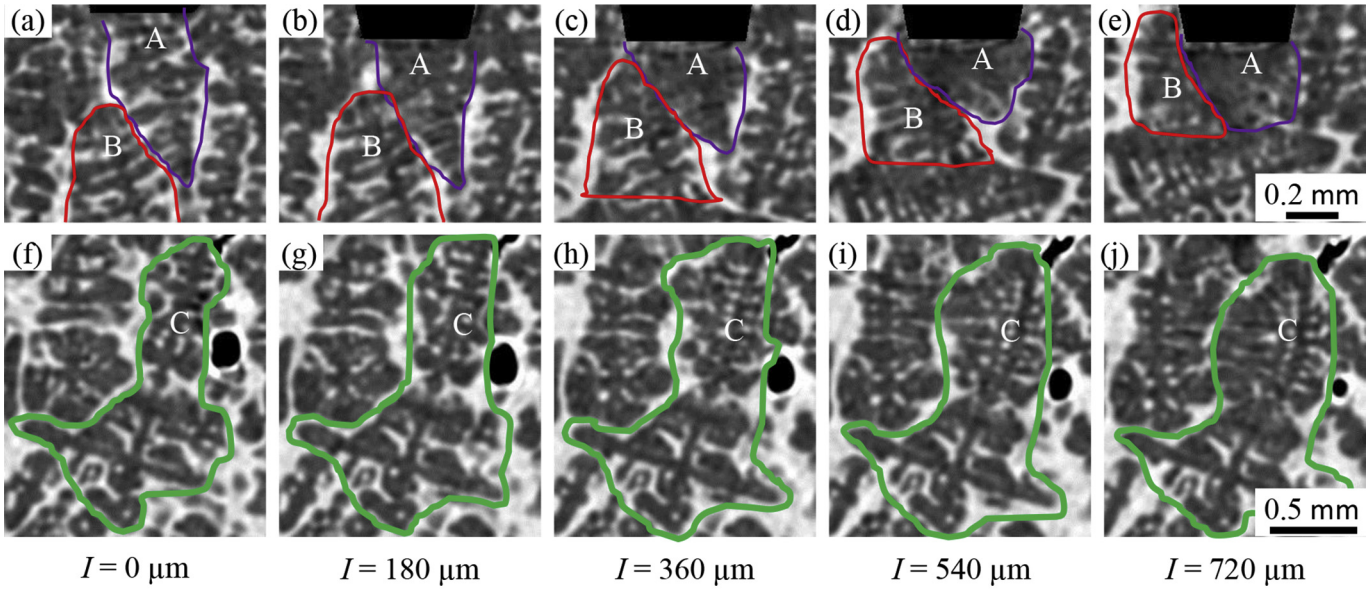

Fig. 8. (a) to (e): Deformation and rearrangement of microstructure beneath the indenter's flat surface; (f) to (j) bending of dendrites.

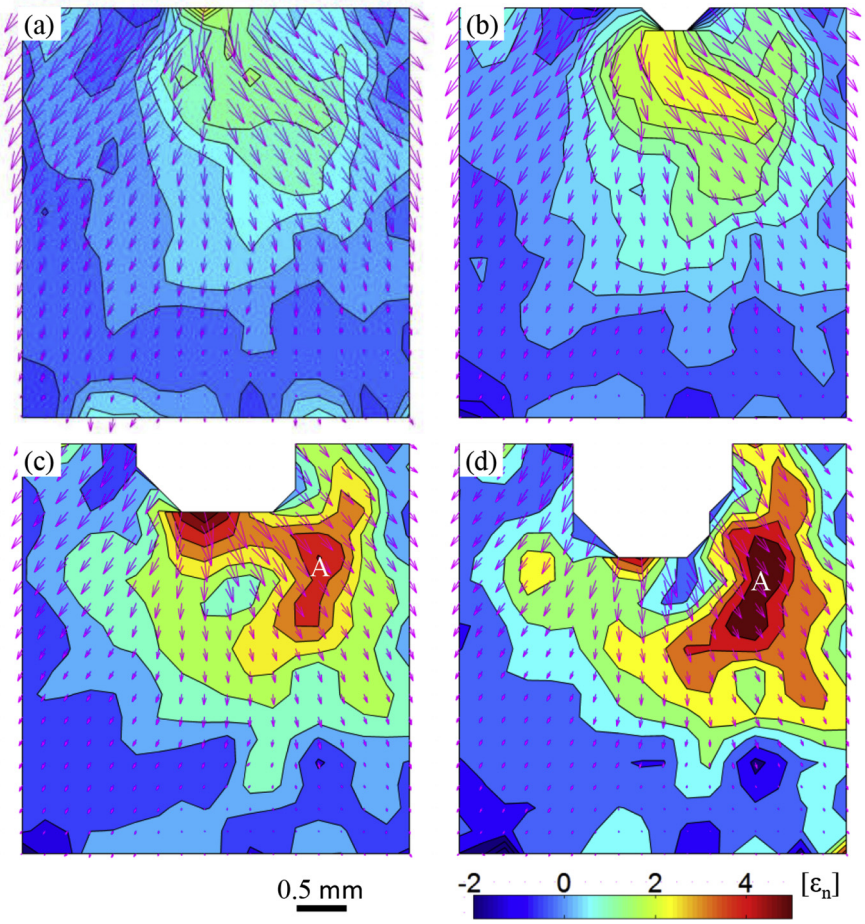

Fig. 9. (a) to (d): Velocity field in the Al–Cu semi-solid specimen when deformed at a displacement rate of 5 μm/s; the imposed contours are the octahedral normal strain map (ε_n) for the following intervals: (a) $I = 0$–90 μm, (b) $I = 0$–180 μm, (c) $I = 0$–360 μm, and (d) $I = 0$–720 μm.

indentation (Fig. 9b), the scope and intensity of dilation increased. At $I = 360$ μm (Fig. 9c), the dilated region, moved to a location slightly away from the indenter (region A), became highly localized and intensified (as also shown in Fig. 9d). Fig. 9d shows that the area of positive ε_n (amount of dilation) reduced under the indenter's flat surface and a small amount of negative ε_n (compressive) appeared.

Fig. 10 (Supplementary movie S4) shows the shear strain (ε_s) map. Unlike the distribution of ε_n (Fig. 9), the shear deformation became more and more intensified below the indenter as the indentation proceeded. A region of high shear strain (over 20% of ε_s) beneath the indenter can be observed in Fig. 10d. This narrow region of shear localization was different from the observations commonly found in semi-solid direct-shear deformation where the localized shear band had a width of a few grains [28,53,54].

Supplementary video related to this article can be found at http://dx.doi.org/10.1016/j.actamat.2015.11.028.

The combined application of time-resolved tomography and digital volume correlation, qualitatively and quantitatively resolves the evolving deformation zone during semi-solid indentaton. *In situ* mapping of localized strain is useful in a wide range of applications from metal formation [47] to food processing [55]. Murthy et al. [47] assessed the evolving two dimensional strain localization during indentation of a Cu sample by particle image velocimetry (PIV, similar to digital image correlation) where the surface textures were tracked. This could not be used to observe strain evolution inside the sample. Waitukaitis and Jaeger [55] also used PIV to track the motion of foreign particles added into a dense suspension. Adding foreign particles, although it enhanced the image contrast for PIV, could change the properties of the suspension. The method used in this study, tracking the microstructural features inherent to the time-resolved X-ray tomographies via DVC, provides the velocity evolution and strain mapping in 3D simultaneously.

4. Conclusions

Deformation zone formation in an equiaxed dendritic semi-solid Al–Cu alloy (solid volume fraction of 72%) occurring though flat-tipped cone indentation was investigated by high speed synchrotron X-ray tomography. Digital volume correlation was used to quantify the velocity field and strain localization throughout the sample. Indentation caused: (1) dilatant granular flow directly related to inhomogeneous deformation, with grain rearrangement via translation and rotation, together with (2) plastic deformation and compaction of individual grains.

The dilatant granular flow caused the enlargement of interdendritic channels localized near the indenter. This also induced migration of interdendritic liquid into this region, and was directly correlated to the DVC measured strain state. The methodology revealed the multitude of deformation mechanisms occurring at a microstructural level, (e.g. dilatancy, liquid flow, macrosegregation, shrinkage voids, and intra-granular deformation), while allowing quantification of the evolution of the strain fields within a complex

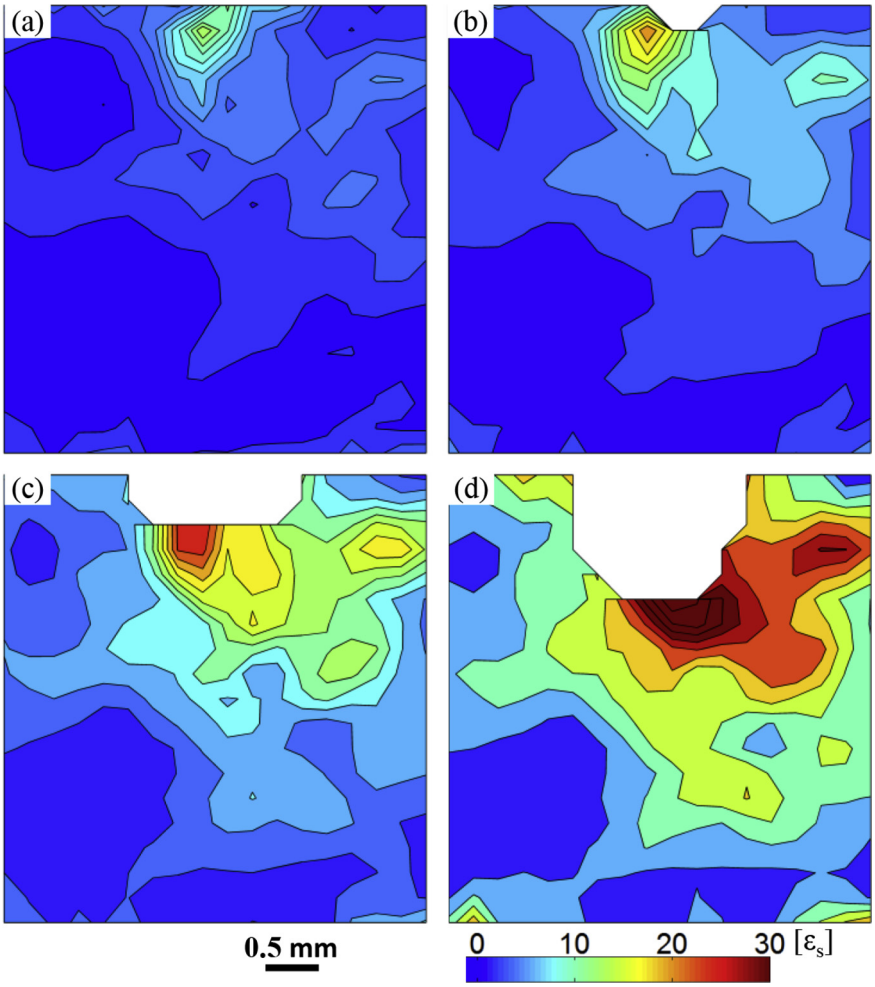

Fig. 10. (a) to (d): Octahedral shear strain map (ε_s): (a) $I = 0–90$ μm, (b) $I = 0–180$ μm, (c) $I = 0–360$ μm, (d) $I = 0–720$ μm.

semi-solid granular material.

Acknowledgements

This work was made possible by the facilities and support provided by the Diamond–Manchester Collaboration and the Research Complex at Harwell, funded in part by the EPSRC (EP/I02249X/1, EP/K007734/1). We thank Diamond Light Source for beamtime (visit EE9018-1), Vision Research UK for the loan of the Miro 310M, and Dr. Robert Atwood for his support during the beamtime. The authors also acknowledge the provision of beamtime 20120463 from the TOMCAT beamline of the Swiss Light Source (Paul Scherrer Institut, Switzerland), and Dr Julie Fife for her support. B.C. thanks General Electric and China Scholarship Council for funding his PhD.

References

[1] L.E. Samuels, T.O. Mulhearn, An experimental investigation of the deformed zone associated with indentation hardness impressions, J. Mech. Phys. Solids 5 (1957) 125–134, http://dx.doi.org/10.1016/0022-5096(57)90056-X.
[2] C.C. Anya, S.G. Roberts, Indentation fracture toughness and surface flaw analysis of sintered alumina/SiC nanocomposites, J. Eur. Ceram. Soc. 2219 (1996) 0–7.
[3] I. Povstugar, P.P. Choi, S. Neumeier, A. Bauer, C.H. Zenk, M. Göken, et al., Elemental partitioning and mechanical properties of Ti- and Ta-containing Co-Al-W-base superalloys studied by atom probe tomography and nano-indentation, Acta Mater 78 (2014) 78–85, http://dx.doi.org/10.1016/j.actamat.2014.06.020.
[4] M. Mostafavi, D.M. Collins, B. Cai, R. Bradley, R.C. Atwood, C. Reinhard, et al., Yield behavior beneath hardness indentations in ductile metals, measured by three-dimensional computed X-ray tomography and digital volume correlation, Acta Mater 82 (2015) 468–482, http://dx.doi.org/10.1016/j.actamat.2014.08.046.
[5] B. Cai, Z.Q. Zheng, D.Q. He, S.C. Li, H.P. Li, Friction stir weld of 2060 Al-Cu-Li alloy: microstructure and mechanical properties, J. Alloys Compd. 649 (2015) 19–27, http://dx.doi.org/10.1016/j.jallcom.2015.02.124.
[6] B. Li, H. Sun, C. Chen, Large indentation strain-stiffening in nanotwinned cubic boron nitride. Nat. Commun. 5 (2014) 4965, http://dx.doi.org/10.1038/ncomms5965.
[7] X. Ma, F. Yoshida, Rate-dependent indentation hardness of a power-law creep solder alloy, Appl. Phys. Lett. 82 (2003) 188, http://dx.doi.org/10.1063/1.1537513.
[8] J. Dean, J. Campbell, G. Aldrich-Smith, T.W. Clyne, A critical assessment of the "stable indenter velocity" method for obtaining the creep stress exponent from indentation data,, Acta Mater 80 (2014) 56–66, http://dx.doi.org/10.1016/j.actamat.2014.07.054.
[9] W.B. Li, J.L. Henshalt, R.M. Hooper, K.E. Easterling, The mechanisms of indentation creep, Acta Metall. Mater 39 (1991) 3099–3110.
[10] T.G. Murthy, Deformation field in indentation of a granular ensemble, Phys. Rev. E 85 (2012) 1–11, http://dx.doi.org/10.1103/PhysRevE.85.061306.
[11] P. Schall, I. Cohen, D.A. Weitz, F. Spaepen, Visualizing dislocation nucleation by indenting colloidal crystals. Nature 440 (2006) 319–323, http://dx.doi.org/10.1038/nature04557.
[12] D. Mueth, G. Debregeas, G. Karczmar, P. Eng, S. Nagel, H. Jaeger, Signatures of granular microstructure in dense shear flows, Nature 406 (2000) 385–389, http://dx.doi.org/10.1038/35019032.
[13] A. Tordesillas, J. Shi, Frictional indentation of dilatant granular materials, Proc. R. Soc. A Math. Phys. Eng. Sci. 455 (1999) 261–283, http://dx.doi.org/10.1098/rspa.1999.0312.
[14] O. Merle, F. Donnadieu, Indentation of volcanic edifices by the ascending magma, Geol. Soc. Lond. Spec. Publ. 174 (2000) 43–53, http://dx.doi.org/

10.1144/GSL.SP.1999.174.01.03.
[15] P.D. Lee, P.E. Ramirez-Lopez, K.C. Mills, B. Santillana, Review: the "butterfly effect" in continuous casting, Ironmak. Steelmak 39 (2012) 244–253, http://dx.doi.org/10.1179/0301923312Z.00000000062.
[16] R. Bigot, V. Favier, C. Rouff, Characterisation of semi-solid material mechanical behaviour by indentation test, J. Mater. Process. Technol. 160 (2005) 43–53, http://dx.doi.org/10.1016/j.jmatprotec.2004.03.016.
[17] E. Hamm, F. Tapia, F. Melo, Dynamics of shear bands in a dense granular material forced by a slowly moving rigid body, Phys. Rev. E - Stat. Nonlinear Soft Matter Phys. 84 (2011) 1–7, http://dx.doi.org/10.1103/PhysRevE.84.041304.
[18] F. Tapia, D. Espíndola, E. Hamm, F. Melo, Effect of packing fraction on shear band formation in a granular material forced by a penetrometer, Phys. Rev. E - Stat. Nonlinear Soft Matter Phys. 87 (2013) 7–10, http://dx.doi.org/10.1103/PhysRevE.87.014201.
[19] W.A. Take, M.D. Bolton, D.J. White, Soil deformation measurement using particle image velocimetry (PIV) and photogrammetry, Géotechnique 53 (2003) 619–631, http://dx.doi.org/10.1680/geot.2003.53.7.619.
[20] Y. Vertyagina, M. Mostafavi, C. Reinhard, R. Atwood, T.J. Marrow, In situ quantitative three-dimensional characterisation of sub-indentation cracking in polycrystalline alumina, J. Eur. Ceram. Soc. 34 (2014) 3127–3132, http://dx.doi.org/10.1016/j.jeurceramsoc.2014.04.002.
[21] B. Cai, S. Karagadde, L. Yuan, T.J. Marrow, T. Connolley, P.D. Lee, In situ synchrotron tomographic quantification of granular and intragranular deformation during semi-solid compression of an equiaxed dendritic Al–Cu alloy, Acta Mater 76 (2014) 371–380, http://dx.doi.org/10.1016/j.actamat.2014.05.035.
[22] L. Yuan, C. O'Sullivan, C. Gourlay, Exploring dendrite coherency with the discrete element method, Acta Mater 60 (2012) 1334–1345, http://dx.doi.org/10.1016/j.actamat.2011.11.042.
[23] K.M. Kareh, P.D. Lee, R.C. Atwood, T. Connolley, C.M. Gourlay, Revealing the micromechanisms behind semi-solid metal deformation with time-resolved X-ray tomography, Nat. Commun. 5 (2014) 4464, http://dx.doi.org/10.1038/ncomms5464.
[24] M. Yamaguchi, C. Beckermann, Simulation of solid deformation during solidification: shearing and compression of polycrystalline structures, Acta Mater 61 (2013) 2268–2280, http://dx.doi.org/10.1016/j.actamat.2012.12.047.
[25] B. Cai, S. Karagadde, D. Rowley, T.J. Marrow, T. Connolley, P.D. Lee, Time-resolved synchrotron tomographic quantification of deformation-induced flow in a semi-solid equiaxed dendritic Al–Cu alloy, Scr. Mater 103 (2015) 69–72, http://dx.doi.org/10.1016/j.scriptamat.2015.03.011.
[26] C.M. Gourlay, A.K. Dahle, Dilatant shear bands in solidifying metals. Nature 445 (2007) 70–73, http://dx.doi.org/10.1038/nature05426.
[27] S. Terzi, L. Salvo, M. Suéry, N. Limodin, J. Adrien, E. Maire, et al., In situ X-ray tomography observation of inhomogeneous deformation in semi-solid aluminium alloys, Scr. Mater 61 (2009) 449–452, http://dx.doi.org/10.1016/j.scriptamat.2009.04.041.
[28] C.M. Gourlay, A.K. Dahle, T. Nagira, N. Nakatsuka, K. Nogita, K. Uesugi, et al., Granular deformation mechanisms in semi-solid alloys, Acta Mater 59 (2011) 4933–4943, http://dx.doi.org/10.1016/j.actamat.2011.04.038.
[29] T. Nagira, C.M. Gourlay, A. Sugiyama, M. Uesugi, Y. Kanzawa, M. Yoshiya, et al., Direct observation of deformation in semi-solid carbon steel, Scr. Mater 64 (2011) 1129–1132, http://dx.doi.org/10.1016/j.scriptamat.2011.03.009.
[30] S. Karagadde, P.D. Lee, B. Cai, J.L. Fife, M. a Azeem, K.M. Kareh, et al., Transgranular liquation cracking of grains in the semi-solid state, Nat. Commun. 6 (2015) 8300, http://dx.doi.org/10.1038/ncomms9300.
[31] J. Fonseca, C. O'Sullivan, T. Nagira, H. Yasuda, C.M. Gourlay, In situ study of granular micromechanics in semi-solid carbon steels, Acta Mater 61 (2013) 4169–4179, http://dx.doi.org/10.1016/j.actamat.2013.03.043.
[32] K.K. McLaughlin, W.J. Clegg, Deformation underneath low-load indentations in copper, J. Phys. D. Appl. Phys. 41 (2008) 074007, http://dx.doi.org/10.1088/0022-3727/41/7/074007.
[33] M. Sistaninia, S. Terzi, A.B. Phillion, J.-M. Drezet, M. Rappaz, 3-D granular modeling and in situ X-ray tomographic imaging: a comparative study of hot tearing formation and semi-solid deformation in Al–Cu alloys, Acta Mater 61 (2013) 3831–3841, http://dx.doi.org/10.1016/j.actamat.2013.03.021.
[34] C. Puncreobutr, P.D. Lee, R.W. Hamilton, B. Cai, T. Connolley, Synchrotron tomographic characterization of damage evolution during aluminum alloy solidification, Metall. Mater. Trans. A 44 (2012) 5389–5395, http://dx.doi.org/10.1007/s11661-012-1563-0.
[35] M. Drakopoulos, T. Connolley, C. Reinhard, R. Atwood, O. Magdysyuk, N. Vo, et al., I12: the joint engineering, environment and processing (JEEP) beamline at Diamond Light Source, J. Synchrotron Radiat. 22 (2015) 1–10, http://dx.doi.org/10.1107/S1600577515003513.
[36] S. Titarenko, P.J. Withers, A. Yagola, An analytical formula for ring artefact suppression in X-ray tomography, Appl. Math. Lett. 23 (2010) 1489–1495, http://dx.doi.org/10.1016/j.aml.2010.08.022.
[37] R.C. Atwood, A.J. Bodey, S.W.T. Price, M. Basham, M. Drakopoulos, A high-throughput system for high-quality tomographic reconstruction of large datasets at diamond Light Source, Philos. Trans. A. Math. Phys. Eng. Sci. 373 (2015), http://dx.doi.org/10.1098/rsta.2014.0398, 20140398–.
[38] N. Otsu, A threshold selection method from gray-level histograms, Syst. Man Cybern. IEEE Trans. 9 (1979) 62–66.
[39] M. Doube, M.M. Kłosowski, I. Arganda-Carreras, F.P. Cordelières, R.P. Dougherty, J.S. Jackson, et al., BoneJ: Free and extensible bone image analysis in ImageJ, Bone 47 (2010) 1076–1079. http://www.sciencedirect.com/science/article/pii/S8756328210014419 (accessed 17.12.13).
[40] O. Reynolds, On the dilatancy of media composed of rigid particles in contact, with experimental illustrations, Philos. Mag. 20 (1885) 470–481.
[41] W.J. Mead, The Geologic Role of Dilatancy, J. Geol. 33 (1925) 685–698.
[42] K. Vo, D.M. Walker, A. Tordesillas, K. Vo, D.M. Walker, A. Tordesillas, Transport pathways within percolating pore space networks of granular materials, AIP Conf. Proc. 551 (2013) 0–4, http://dx.doi.org/10.1063/1.4811990.
[43] T. Nagira, S. Morita, H. Yokota, H. Yasuda, C.M. Gourlay, M. Yoshiya, et al., Situ observation of deformation in semi-solid Fe-C alloys at high shear rate, Metall. Mater. Trans. A 45 (2014) 5613–5623, http://dx.doi.org/10.1007/s11661-014-2489-5.
[44] N.S. Barekar, B.K. Dhindaw, Twin-roll casting of aluminum alloys – an overview, Mater. Manuf. Process 29 (2014) 651–661, http://dx.doi.org/10.1080/10426914.2014.912307.
[45] P.D. Lee, A. Chirazi, D. See, Modeling microporosity in aluminum–silicon alloys: a review, J. Light Met. 1 (2001) 15–30. http://www.sciencedirect.com/science/article/pii/S1471531700000031 (accessed 14.12.13).
[46] M. Yun, S. Lokyer, J. Hunt, Twin roll casting of aluminium alloys, Mater. Sci. Eng. A 280 (2000) 116–123, http://dx.doi.org/10.1016/S0921-5093(99)00676-0.
[47] T.G. Murthy, C. Saldana, M. Hudspeth, R.M. Saoubi, Deformation field heterogeneity in punch indentation, Proc. R. Soc. A 470 (2014) 1–17.
[48] W. Johnson, P.P.B. Mellor, Engineering Plasticity, Ellis Horwood Limited, 1983.
[49] G. Reinhart, H. Nguyen-Thi, N. Mangelinck-Noël, J. Baruchel, B. Billia, In situ investigation of dendrite deformation during upward solidification of Al-7wt.%Si, Jom 66 (2014) 1408–1414, http://dx.doi.org/10.1007/s11837-014-1030-z.
[50] J.W. Aveson, G. Reinhart, H. Nguyen-Thi, N. Mangelinck-Noël, N. D'Souza, H.J. Stone, Origins of misorientation defects in single crystal castings: a time resolved in situ synchrotron X-ray radiography study,, MATEC Web Conf. 14 (2014) 05003, http://dx.doi.org/10.1051/matecconf/20141405003.
[51] D. Fuloria, P.D. Lee, An X-ray microtomographic and finite element modeling approach for the prediction of semi-solid deformation behaviour in Al–Cu alloys, Acta Mater 57 (2009) 5554–5562, http://dx.doi.org/10.1016/j.actamat.2009.07.051.
[52] M. Yamaguchi, C. Beckermann, Direct numerical simulation of solid deformation during dendritic solidification, Jom 66 (2014) 1431–1438, http://dx.doi.org/10.1007/s11837-014-1001-4.
[53] C.M. Gourlay, T. Nagira, A.K. Dahle, N. Nakatsuka, K. Uesugi, H. Yasuda, Synchrotron radiography of direct-shear in semi-solid alloys, IOP Conf, Ser. Mater. Sci. Eng. 27 (2012) 012086, http://dx.doi.org/10.1088/1757-899X/27/1/012086.
[54] T. Nagira, H. Yokota, S. Morita, H. Yasuda, M. Yoshiya, C.M. Gourlay, et al., Characterization of shear deformation based on in-situ observation of deformation in semi-solid Al – Cu alloys and water-particle mixture, ISIJ Int. 53 (2013) 1195–1201.
[55] S.R. Waitukaitis, H.M. Jaeger, Impact-activated solidification of dense suspensions via dynamic jamming fronts, Nature 487 (2012) 205–209, http://dx.doi.org/10.1038/nature11187.